POSITIVE-ION/NEGATIVE-ION COINCIDENCE (PINICO) EXPERIMENTS ON WATER

Bruno Moog

Master's thesis
MAXM30
Supervisor: Rami Sankari
Co-supervisor: Antti Kivimäki
Autumn 2016

LUND UNIVERSITY

Hâtez-vous lentement, et sans perdre courage,
Vingt fois sur le métier remettez votre ouvrage,
Polissez-le sans cesse, et le repolissez,
Ajoutez quelquefois, et souvent effacez.

Nicolas Boileau
L'art poétique -1674.

Make haste slowly, and from danger never shirk,
As twenty times over you revise your work,
Polishing, polishing, day after long day,
Sometimes adding, and often taking away.

Nicolas Boileau,
The poetic art -1674.

Abstract

A new setup for versatile ion time-of-flight coincidence spectroscopy was built using a pre-existing negative ion time-of-flight spectrometer aligned with a short extension that may be used to detect photons, Auger electrons or positive ions. The extension was designed to be short to improve detection of photons, as they do not have a preferred direction for their emission, and high-momentum particles, which would miss the detector if it were placed farther from the interaction region. This new setup was tested for Positive-Ion/Negative-Ion Coincidence experiments near the O1s absorption edge of water. Positive ion detection was used as the start signal, due to the shorter time of flight in the short extension than in the negative ion time-of-flight spectrometer. The improvement of the setup in terms of high-momentum positive ions detection comes at the expense of resolution, and the use of positive ions as the start signal results in the absence of positive ion/electron coincidences in the spectrum.

The O^+/H^-, O^{++}/H^- and the H^+/H^- coincidence peaks were observed, and identified as real peaks via the change in their position when the applied voltages in the experimental setup were varied. Their attribution was made so that they are consistent with one another for their intensity and position. The ion pair yields were then studied and used to discuss the dissociation pathways of water after O1s core ionization. The three dominant photoexcitation peaks of water ($4a_1$ $2b_2$ and $2b_1$) and the above threshold regime past 539.9eV were visible for each of the ion pairs. The high acceptance of the short extension enabled the detection of a larger number of H^+ ions, resulting in clearly visible resonances above threshold, which can be attributed to simultaneous excitation of a O1s core electron and a valence electron. The H^+/O^- yield showed a lower energy resonance with a double peak structure that was not visible in the resonances in the yield of the other ion pairs at higher energy.

Acknowledgements

During the course of this work, I had the opportunity to meet and work with remarkable people who are renowned contributors to their field. They have been a great source of support and advice, which has been essential to the accomplishment of this work, and I want to express my sincere gratitude towards them. In particular, I would like to thank my supervisor Rami Sankari and my co-supervisor Antti Kivimäki for patiently correcting my manuscript and consistently guiding me towards improvement. I was given the opportunity to work at the Elettra Syncrotrone in Trieste, by becoming part of a research team composed of Christian Stråhlman, Robert Richter and Antti Kivimäki. They all have been very generous with their time and efforts in making this experiment a success. Individually, they have kindly provided me with their insight and advice when it appeared to be needed, enabled me to learn as much as possible from this experience, and made me play an active and relevant part in this team effort in a very exciting and advanced field of research.

Thank you all very much.

Contents

List of abbreviations

AEPICO   Auger Electron/Positive Ion Coincidence

AENICO   Auger Electron/Negative Ion Coincidence

AES   Auger Electron Spectroscopy

AEPECO   Auger Electron/Photoelectron Coincidence

FS   Fluorescence Spectroscopy

MCP   Micro Channel Plate

NIPICO   Negative Ion/Positive Ion Coincidence

NIPIPICO   Negative Ion/Positive Ion/Positive Ion Coincidence

PEPICO   Photoelectron/Photoion Coincidence

PINICO   Positive Ion/Negative Ion Coincidence

TOF   Time-of-Flight

TOFMS   Time-of-Flight Mass Spectroscopy

XENICO   X-ray Emission/Negative Ion Coincidence

XEPICO   X-ray Emission/Positive Ion Coincidence

XPS   X-ray Photoelectron Spectroscopy

1 Introduction

The study of water has been the focus of a large quantity of scientific work. In chemistry, water is commonly used as a solvent, as its polar character makes it an excellent choice for the dissolution of ionic compounds. It is also a necessary participant in an extremely large number of chemical reactions. In biology, the varying energetic stability of molecules dissolved in water is responsible for the formation of lipids bilayers and micelles that are essential for life. In atmospheric sciences, it is is a key compound in understanding climate dynamics as it is the most abundant greenhouse gas. And in thermodynamics, it has a remarkably high heat capacity, a high freezing point and a high boiling point, making it an excellent heat regulator. These few properties find their source at the molecular level. And in contrast to its size and apparent simplicity, the behavior of the water molecule still needs to be fully understood[1].

Among the most prominent means of investigation available for studying the behavior and properties of molecules is ion time-of-flight mass spectroscopy (TOFMS), whereby ionization of the molecule is used as a probing mechanism, and the fragments of the molecule produced, most commonly positive ions, have their mass to charge ratio measured. This is employed as an indirect means to better understand the behavior of the original molecule. Coincidence detection techniques of various fragments have been developed and used to extract more information from the ionization process in TOFMS. In particular, Negative Ion/Positive Ion Coincidence (NIPICO) apparatus was developed recently and used to study the water molecule at the Gas Phase photoemission beamline of Elettra, the Italian synchrotron located in Trieste[2, 3].

This work reports assembling and testing a newly developed extension for this apparatus, referred to as the ABC extension, which is meant to replace the positive ion time-of-flight (TOF) spectrometer known as RamiTOF in the existing NIPICO setup of the Gas Phase photoemission beamline. This extension should enable an increased ion yield, as well as improve the flexibility of the setup by allowing X-ray Emission/Negative Ion Coincidence (XENICO), Auger Electron/Negative Ion Coincidence (AENICO), and Positive Ion/Negative

Ion Coincidence (PINICO) experiments. Coincidence spectroscopy is performed on water in order to check that the extension works as expected, to reproduce and improve previous results using a different setup, and to verify experimental predictions.

2   Molecular theory of water

The water molecule has a tetrahedral structure centered around the oxygen atom, with two hydrogen ligands and two lone pairs of electrons (four in total), effectively forming a 104.5° bent molecule, as illustrated in Figure 1. The bend is caused by the two lone pairs on the oxygen atom repelling the electron density in the two covalent bonds with hydrogen. This bend is responsible for the non-zero permanent dipole moment of the molecule, making water a polar molecule.

The water molecule can be categorized as being part of the C_{2v} point group in terms of symmetry, where C represents the rotational axis of the molecule. The axis is chosen as the one that enables the smallest rotation producing an indistinguishable molecule. For water, the rotational axis lies in the plane of the molecule and through the oxygen. The corresponding angle of rotation provides the next term by taking the ratio 2π over the rotation angle: $\frac{2\pi}{\pi} = 2$. The v subscript signifies that the molecule also possesses at least one plane of symmetry that contains the principal axis of rotation. Water has two, one in the plane of the molecule and a second one perpendicular to it. As a non-linear molecule, water has 3N-6 (where N is the number of atoms in the molecule) vibrational modes: one where the bonds are stretched symmetrically, one where they are stretched asymmetrically and one where the bend angle varies. Due to its lack of axial symmetry, the water molecule also has 3 rotational modes, one along each Cartesian axis[4].

The hydrogen atoms forming covalent bonds with a more electronegative oxygen atom leaves them with a small positive net charge. This positively charged hydrogen can establish electrostatic bonds with lone electron pairs carried by other atoms or molecules. A water molecule can thus create hydrogen bonds with other water molecules. Hydrogen bonds are
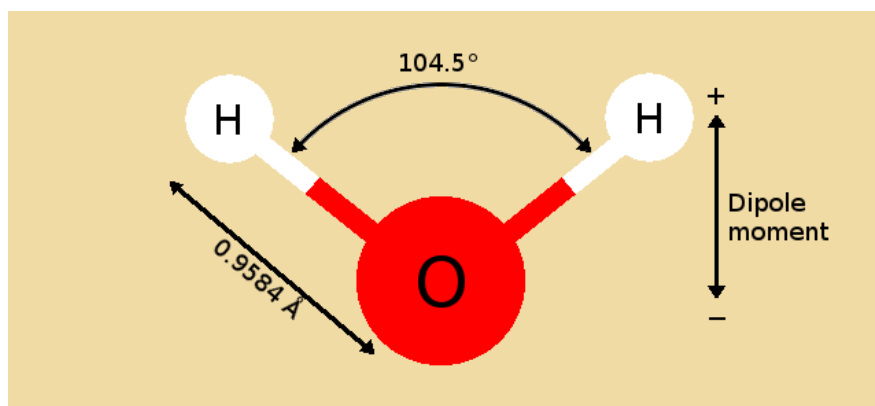
Figure 1: Geometry of the water molecule.

relatively weaker and longer bonds (20 to 30 $kJ \cdot mol^{-1}$ and 0.25 to 0.3nm) than covalent or ionic bonds (several hundreds $kJ \cdot mol^{-1}$ and approximately 0.1nm)[1]. The ability of water to create hydrogen bonds with other compounds increases its usefulness as a solvent. In liquid water, this is responsible for a high heat capacity and surface tension, via the increase of the energy required to separate each molecule from its neighbours. Hydrogen bonds are also a key parameter in the structure of cubic ice, explaining the lower density of solid water to that of liquid water, which is a very uncommon property among chemical compounds.

2.1 The molecular orbitals of water

In a molecule, the atomic orbitals combine to form molecular orbitals. The properties of these molecular orbitals strongly depend on the atomic orbitals they originate from, for both their shape and their energy. In particular, the combination of two atomic orbitals give two molecular orbitals: one bonding, that combines in phase, and one antibonding, that combines out of phase and has a higher energy. The resulting interactions are respectively increasing and decreasing the overall stability of the molecule. This means that depending on the molecular orbitals in which the electrons are located, the molecule may or may not be stable. For example the H_2 molecule is stable in its ground state, because the two available electrons fill the $\sigma_g 1s$ bonding orbital, leaving the higher energy $\sigma_u^* 1s$ antibonding orbital unoccupied. In contrast, the He_2 molecule is unstable in its ground state, because the four

electrons available fill both the $\sigma_{\mathrm{g}}1s$ and the $\sigma_{\mathrm{u}}^{*}1s$ which cancel each other out, thus preventing molecular bonding in the ground state. In this notation, σ denotes that the orbital is symmetric with respect to the internuclear axis. g or u stand for "gerade" and "ungerade", meaning that inversion through the center of symmetry of the molecule produces the same phase or the opposite phase respectively. And the presence of a star, $*$, denotes the anti-bonding nature of the orbital. There also are conditions that need to be fulfilled for atomic orbitals to hybridize and form molecular orbitals. Namely, they must have similar energies, they must have a sufficient overlap, and they must have the same symmetry with respect to the internuclear axis[4]. The electronic structure of water in the ground state can be written as[5]:

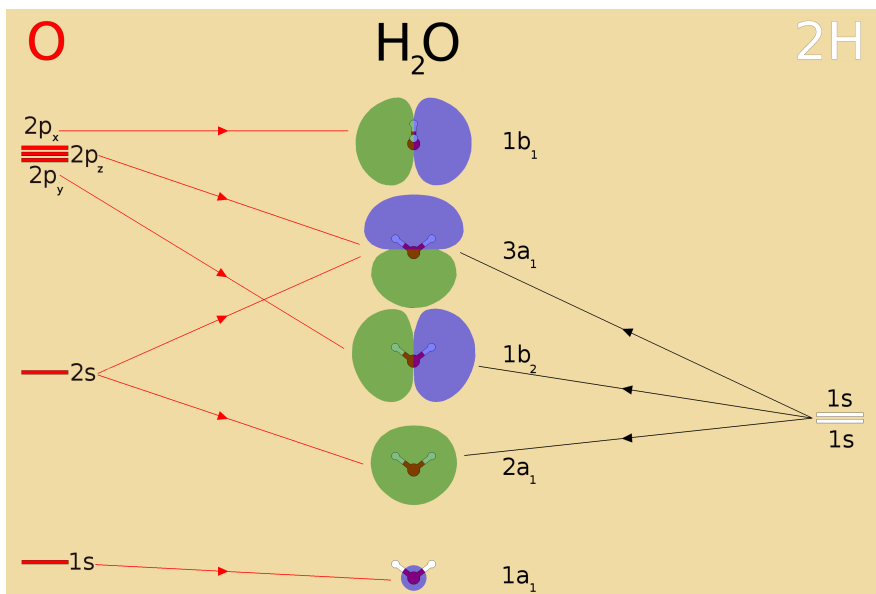$$(1a_1)^2(2a_1)^2(1b_2)^2(3a_1)^2(1b_1)^2$$

Figure 2: The combination of the atomic orbitals of oxygen and hydrogen to produce the molecular orbitals of water.

These molecular orbitals are represented in Figure 2. The original $2p_x$, $2p_y$ and $2p_z$ of oxygen interact differently with the 1s orbitals of the two hydrogen atoms due to their orientation. The $2p_x$ orbital is perpendicular to the molecular plane, and its lack of common symmetry with the 1s orbitals of the two hydrogen atoms prevents it from being successfully

hybridized. Indeed, when brought closer together, the positive part of the $2p_x$ wavefunction overlaps with the 1s hydrogen orbital exactly as much as the negative part of the $2p_x$ wavefunction does with the 1s hydrogen orbital, and the two overlaps cancel each other out. The $2p_x$ orbital of oxygen therefore becomes the $1b_1$ orbital of water with 100% O2p character. On the other hand, the two other 2p orbitals of oxygen, $2p_y$ and $2p_z$, can have an overlap with the 1s orbitals of the hydrogen atoms which is not cancelled by symmetry, and they participate in the hybridized molecular orbitals $3a_1$ and $1b_2$. The resulting $1b_2$ molecular orbital is a mixture of 41% H1s and 59% O2p, while the $3a_1$ orbital is 17% H1s, 10% O2s and 72% O2p[6]. The 2s orbital of oxygen and the 1s orbitals of the hydrogens have close enough energies to also allow for molecular hybridization in the $3a_1$ and the $2a_1$ orbitals of water. The 1s orbital of oxygen, however, has an excessive energy difference with the 1s orbitals of the hydrogens, preventing it from being hybridized as well. It becomes the $1a_1$ orbital of water, which is often referred to as the O1s orbital, as it is not hybridized and retains 100% of the original character of the 1s orbital of oxygen.

2.2   Light-matter interaction

The dominant electronic process which results from the interaction of gaseous water with X-rays with an energy of around 540eV is photoabsorption, with the formation of a core electron hole, specifically in the O1s shell[7]. The various spectroscopic processes that may occur across the energy spectrum are shown in Figure 3. Other processes that become more important at high photon energies such as inelastic (Compton) and elastic (Thompson) scattering can be neglected here[8].

The O1s electron can either be ionized or excited. The lifetimes of such core hole states are extremely short, at around 3.3fs[10]. These unstable states decay by the transition of an electron from one of the outer shells that falls down to fill the hole. The transition probability depends on the molecular orbital giving an electron. For water, the O2p character of the molecular orbital correlates positively with the strength of the transition[11]. The energy that accompanies this transition can be released in two different forms, which are the ejection of
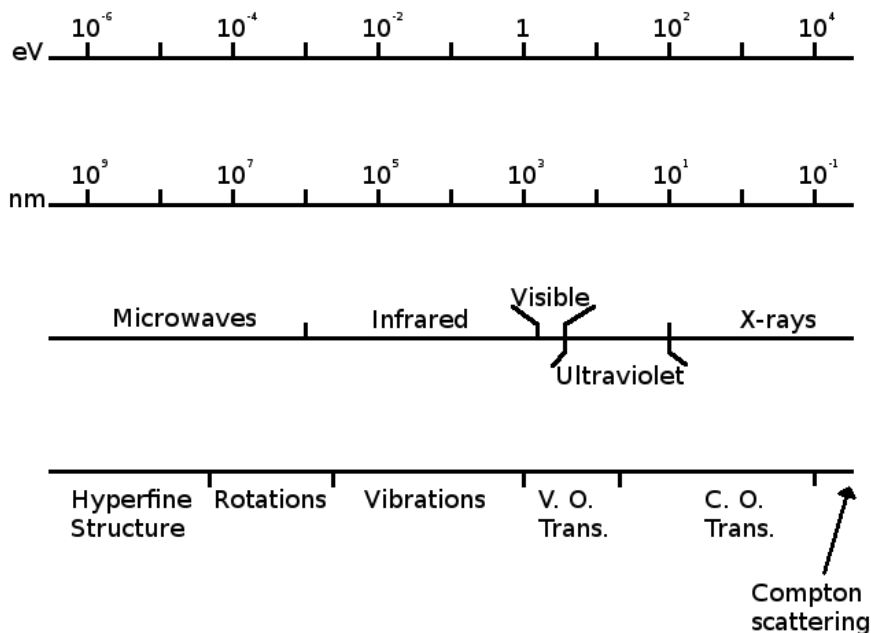
Figure 3: Energy of the light used, associated wavelength and corresponding dominant processes[9]. V.O. stands for valence orbital and C.O. for core orbital.

another electron or the emission of a fluorescence photon, as illustrated in Figures 4 and 5.

The first of these two processes that releases energy from the molecule is referred to as Auger decay, where the energy release connected to the outer electron's transition is transferred to another electron, which is then ejected from the atom or molecule; this is a very simplified model, but it is sufficient for this work. The fact that an electron is ejected as a consequence of the absorption of X-rays makes Auger decay a subset of the commonly known photoelectric effect. Auger decay has a higher probability to occur in light elements rather than heavy elements, as can be seen in Figure 6. The data used for the radiative decay yield was obtained from the fitting of "most reliable experimental yields" performed by Bambynek *et al.*[12]. The data for the nonradiative decay yield was produced by substracting the fluorescence (radiative) yield from 1.

Which electron is most likely to be ejected in this manner depends on the specific electronic structure of the molecule. For gaseous water, simple measurement of the kinetic energies of
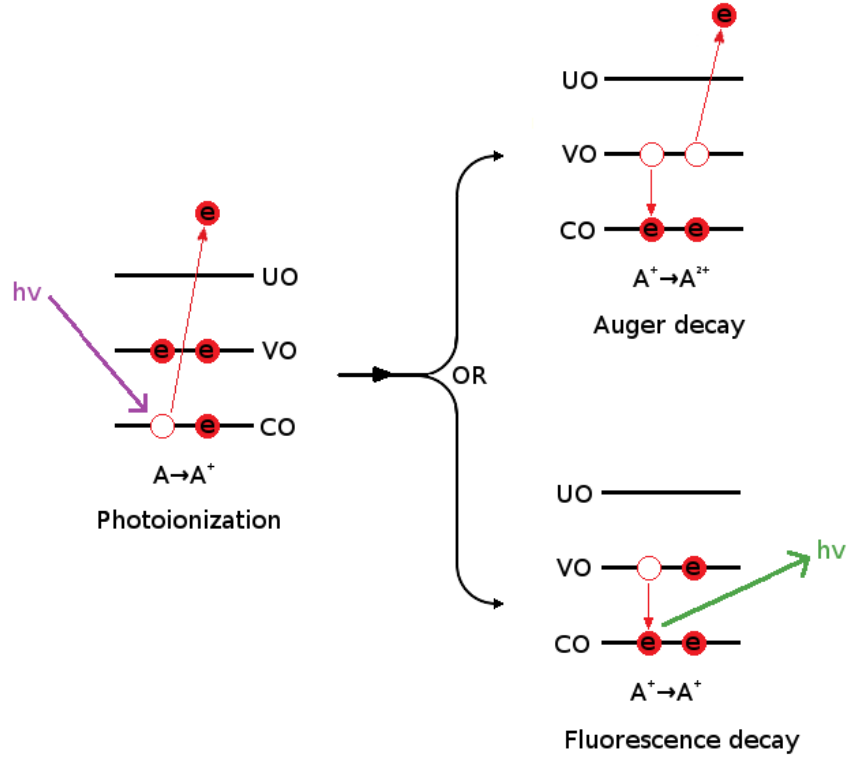
Figure 4: Main types of energy relase after photoionization of a core electron. CO stands for core orbital, VO for valence orbital and UO for unoccupied orbital.

the emitted (secondary) electrons provides information about the corresponding electron configurations[5, 7, 13]. The energy of the Auger electron can be roughly estimated via the formula: $E_{Auger} \approx E_{Core} - E_1 - E_2$, where E_1 and E_2 are the orbital energies of the final valence holes produced by Auger decay. If the species undergoing Auger decay is ionized in the first step, it is referred to as non-resonant or normal Auger decay. If it is a neutral molecule that had one of the core electrons excited to an unoccupied shell but is still bound, it is referred to as resonant Auger decay, both processes are shown in Figures 4 and 5.

The other decay process, referred to as radiative (or fluorescence) decay, is the release of this energy in the form of a photon, which is also described in Figures 4 and 5. As it is competing with Auger decay, it is more likely to occur in core ionized heavy elements than in light elements as shown in Figure 6. The K X-ray fluorescence emission spectrum of water, which corresponds to a transition from a valence orbital to a core hole, has been successfully
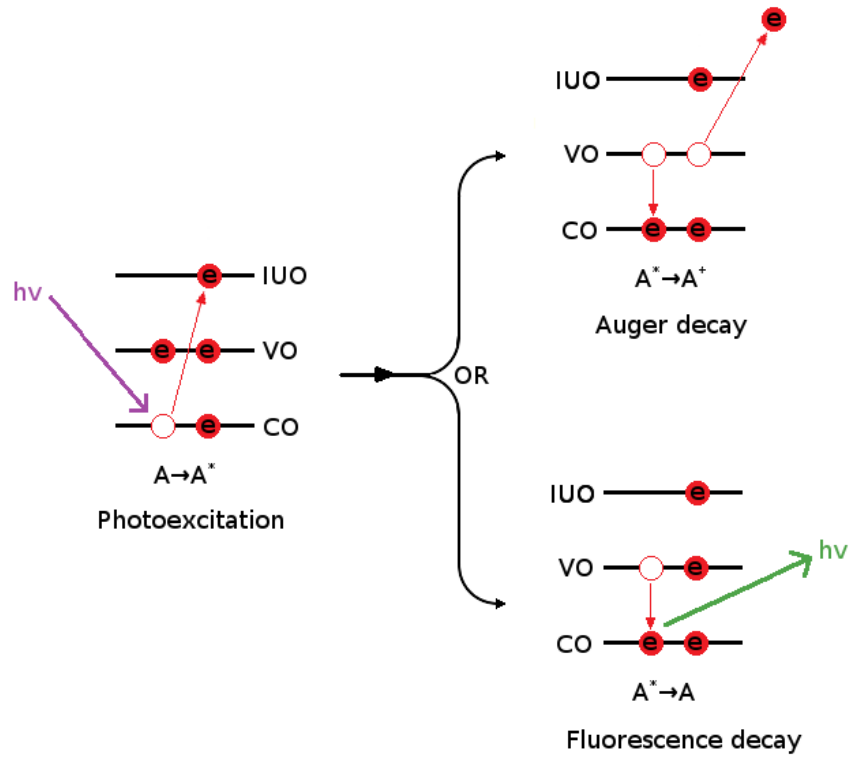
Figure 5: Main types of energy relase after photoexcitation of a core electron. CO stands for core orbital, VO for valence orbital and IUO for initially unoccupied orbital.
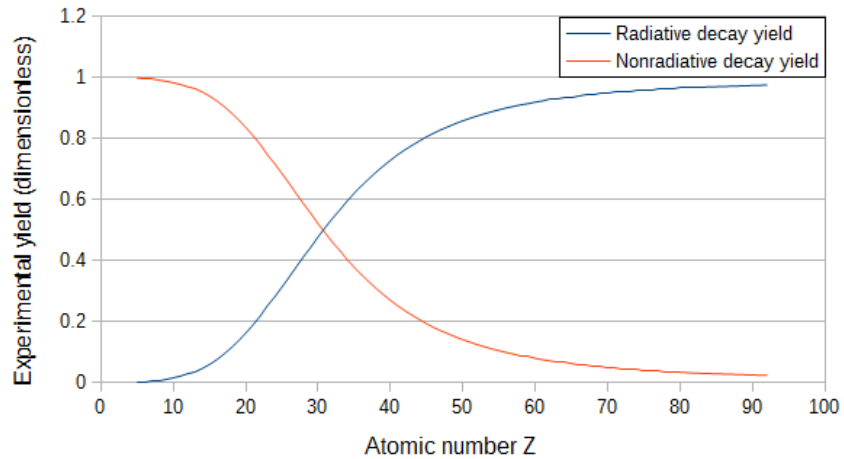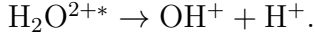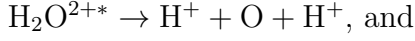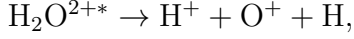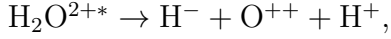

Figure 6: Yield of fluorescence decay (radiative) and Auger decay(nonradiative) in the case of K-shell ionization as a function of the atomic number of the excited species. Data obtained from Bambynek *et al.*[12].

studied in earlier work[14].

Following these processes, the excited or ionized water molecule can break into charged fragments, which can then be accelerated, separated and detected using standard Time-of-Flight Mass Spectroscopy (TOFMS). According to previous studies[14, 15] and theoretical models[11], the most likely electron giver in the relaxation process is the $1b_1$ shell, as it has a strong 2p character. It is also centered on the oxygen, like the $1a_1$ shell in which the hole occurs, and this increases the overlap between the two wavefunctions. The $1b_2$ and $3a_1$ shells are the two main orbitals responsible for the covalent bonding between the oxygen atom and the two hydrogen atoms, which decreases their probabilities as electron donor in the stabilization process. Finally, the contribution of the $2a_1$ orbital is heavily suppressed due to the application of selection rules. In particular, atomic dipole selection rules still apply to this transition due to the strong O2s and O1s character of $2a_1$ and $1a_1$ respectively[15].
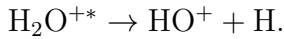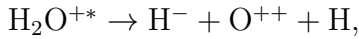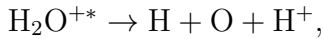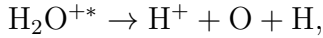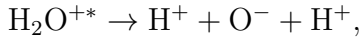
For the water molecule, one can distinguish four different possibilities of ion fragmentation channels following normal Auger decay. In the following equations * and ** denote a valence and core excited species, respectively.

After $H_2O^{+**} \rightarrow H_2O^{2+*} + e^-$, the simple linear dissociation pathways are:

$H_2O^{2+*} \rightarrow H^- + O^{++} + H^+$,

$H_2O^{2+*} \rightarrow H^+ + O^+ + H$,

$H_2O^{2+*} \rightarrow H^+ + O + H^+$, and

$H_2O^{2+*} \rightarrow OH^+ + H^+$.

One can notice that none of these processes can produce O^-, and only one can produce H^-. If an O^- ion is produced above the ionization threshold, it has to originate from more complex processes than the ones described here.

For resonant Auger decay, after $H_2O^{**} \rightarrow H_2O^{+*} + e^-$, the simple linear dissociation pathways are:

$H_2O^{+*} \rightarrow H^- + O^+ + H^+$,

$H_2O^{+*} \rightarrow H^+ + O^- + H^+$,

$H_2O^{+*} \rightarrow H^+ + O + H$,

$H_2O^{+*} \rightarrow H + O + H^+$,

$H_2O^{+*} \rightarrow H^- + O^{++} + H$,

$H_2O^{+*} \rightarrow HO + H^+$, and

$H_2O^{+*} \rightarrow HO^+ + H$.
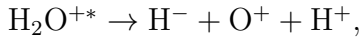
For resonant Auger decay, one of these processes results in O^- and another in H^-. Autoionization and electron recapture increase the number of possibilities for dissociation for both resonant and non-resonant Auger decay.

For radiative decay of core ionized water, $H_2O^{+**} \rightarrow H_2O^{+*} + h\nu_{\text{fluorescence}}$, the possible resulting ions following simple linear dissociation are the same as for resonant Auger decay, since it produces the H_2O^{+*} ion before the eventual breakdown, the only difference being that a fluorescence photon is emitted instead of an Auger electron. This leaves the fragments with only one positive change imbalance above the ionization threshold, which would be an interesting phenomenon to monitor via the detection of the emitted photons. As water is composed of light elements (Z<10), fluorescence decay should be a measurable, but rare event[14].

3 Methods and instrumentation

3.1 Synchrotron radiation

Synchrotron radiation facilities are built around storage rings, which are circular particle accelerators for electrons that use the local acceleration of these charged particles to produce light. The electrons are kept in the storage ring, circulating at nearly the speed of light. This high speed is required to take advantage of the correlation between the energy of the electrons and the power and energy of the light that can be produced by deviating their trajectories. Modern synchrotron radiation facilities aim at producing and concentrating light, in particular X-rays, by placing insertion devices along the path of the electrons. These insertion devices called wigglers and undulators act as lightsources by making the electron path briefly oscillate in the plane of the storage ring. Beamlines which are tangential to the storage ring guide the produced light towards the experiments. They also monochromatize and spatially focus the light so that it is usable at experimental endstations, where the samples are studied.

Synchrotron radiation is a remarkable tool for X-ray based light-matter interaction experiments due to its unique properties, like high flux, which enables a much more rapid collection of experimental data, high brilliance, which allows to concentrate the light produced in a narrow beam with low divergence, high wavelength and polarization tunability, and high temporal stability. In addition, all of these characteristics can be modified at each beamline independently of the others. This makes synchrotron facilities research hubs that are the ideal location for scientific investigation as well as the development of new instrumentation and techniques.

The first generation of synchrotron radiation facilities was developed based on the incidental production of synchrotron radiation that occurs when a high-speed stream of charged particles is deviated, in storage rings that were primarily designed for high-energy and nuclear physics experiments, in the 1960s. As such, the first generation of synchrotron radiation sources was referred to as parasitic facilities. The appearance of dedicated facilities

later defined the second generation of synchrotron radiation sources in the 1980s. The third generation sources are characterized by the fact that the storage rings have been specifically designed with straight sections for insertion devices, such as wigglers or undulators, that are used to optimize the brightness of the light produced. This third generation started in the 1990s and is still operating. Their development has recently led up to the first fourth generation light sources, such as free electron lasers and diffraction limited storage rings, and in particular with the opening of the MAX IV synchrotron radiation facility in Lund, Sweden.

This experimental work was performed using the Gas Phase photoemission beamline at the Elettra synchrotron in Trieste, Italy. The Elettra facility is a third generation synchrotron. It was built in 1993 and provides its 25 operating beamlines with radiation ranging from the infrared to hard X-rays. It operates in top-up mode since 2010, which means that the current circulating in the accelerator is kept close to constant by injecting additional electrons into the storage ring at regular intervals. This is necessary due to unavoidable losses in the accelerator slowly depleting the current stored[16].

3.2   The Gas Phase photoemission beamline at Elettra

The Gas Phase photoemission beamline at Elettra was designed for atomic and molecular spectroscopy of gaseous compounds. It is built around an undulator providing an energy range spanning 13 to 900eV. A variable angle spherical grating monochromator with 5 interchangeable gratings provides a high resolving power, $\frac{E}{\Delta E}$, of 10000 or higher for most of the working photon energy range. The focused spot size at the sample is around 200μm in diameter and it has a 3mrad divergence[16, 17].

The beamline was initially designed with two end stations, one for electron-electron coincidence experiments and another for angle-resolved photoemission spectroscopy[18]. Most importantly, however, it provides the opportunity for users to set up their own chamber, which makes it one of the most flexible beamlines at the Elettra synchrotron, and a good location for testing custom made instruments.

3.3   Time-of-flight mass spectroscopy

This experiment is based on ion TOFMS, which is used to determine the mass to charge ratio of the ions hitting the detector, for example those of ionic fragments produced when a molecule under study dissociates.

TOFMS is performed as follows. First, ions are produced by direct or indirect ionization (resonant Auger decay, for example). The energy required to initiate ionization can be provided in a number of ways, such as a particle beam (most commonly electrons) or a laser beam. In this case, the energy was provided by X-rays with a carefully selected wavelength, in order to specifically ionize or excite the innermost electrons of the water molecule. After that, the molecules break apart into positive ions, negative ions, neutral fragments and electrons. The resulting ions are subjected to an electric potential that accelerates them, giving them an energy of $q \cdot U$ where q is their charge and U is the electric potential applied to them, or in terms of kinetic energy $\frac{1}{2}m \cdot v^2$. As a consequence, this electric potential will accelerate the ions differently based on their mass to charge ratio, which thus correlates with the speed acquired by the ions exiting the acceleration region $v_{\text{final}} = \sqrt{2} \cdot \sqrt{U \cdot \frac{q}{m}}$. After that, the ions proceed to a drift tube, in which they temporally separate due to their different velocities. Finally, the time of flight of the ions is measured as a time difference of some start pulse, and the moment they reach the detector. This allows to distinguish their mass to charge ratio, and as a consequence to identify them ($t = \frac{d}{v_{\text{final}}}$ and therefore $t = \frac{d}{\sqrt{2U}} \cdot \sqrt{m/q}$). The ions can also be counted, as their relative quantity provides key information about the likelihood of the different fragmentation processes. This information can then be linked back to their structural and chemical properties.

The volume in which ionization occurs, the temperature of the chemicals ionized, the various direction and speed of motion of the ions produced are some of the key parameters that limit the precision of a time-of-flight (TOF) spectrometer. These sources of error can be corrected by respectively reducing the interaction volume, cooling the chemicals and using energy focusing techniques. As a consequence, the structure of most TOF spectrometers, including the one at the Elettra Gas Phase photoemission beamline, is slightly more complex.

This TOF spectrometer design has two different regions with a smaller electrical field in the source region, followed by a higher field in the acceleration region leading up to the field free drift region[19]. This structure, known as the Wiley-McLaren two-step TOF spectrometer is typically used because it has good mass resolution due to space focusing[20].

TOF spectrometers are most commonly used to measure positive ions. There are two main motivations for it, the first being the much higher proportion of positive ions to that of negative ions. Indeed, the breaking down of neutral molecules and atoms into ions is commonly accompanied by the production of free electrons, which leads to the overall charge of the remaining ionic products being positive. Detection of positive ions is therefore more common and can be used to study a larger proportion of ionic breakdown pathways. Also, the production of a large amount of electrons in the ionization process results in large noise if the negative ions are the ones measured via TOFMS. This is not an issue for positive ions, as electrons and positive ions go in opposite directions. However, techniques have been developed to reduce the issue caused by the presence of electrons in negative ions TOFMS, enabling the measurement of negative ions without an excessive number of hits from the electrons[21]. As fewer ionization pathways can produce these negative ions, they are highly specific, making them sensitive probes for weaker processes.

3.4 Coincidence spectroscopy

In TOF spectroscopy, some information is lost due to the often incomplete detection of all emitted particles. Coincidence spectroscopy, on the other hand, can be used to gain more information from the detected particles. It also enables a synergistic use of the data of the different spectroscopic techniques used, which results in a much more precise identification of the ionic fragmentation processes. It has been implemented in a number of different ways as is illustrated in Figure 7.

Using Auger Electron Photoelectron Coincidence (AEPECO), the photoelectron emitted during the initial creation of the core hole in the innermost shell and the Auger electron emitted afterwards have been coincidentally studied in order to identify with higher precision

18
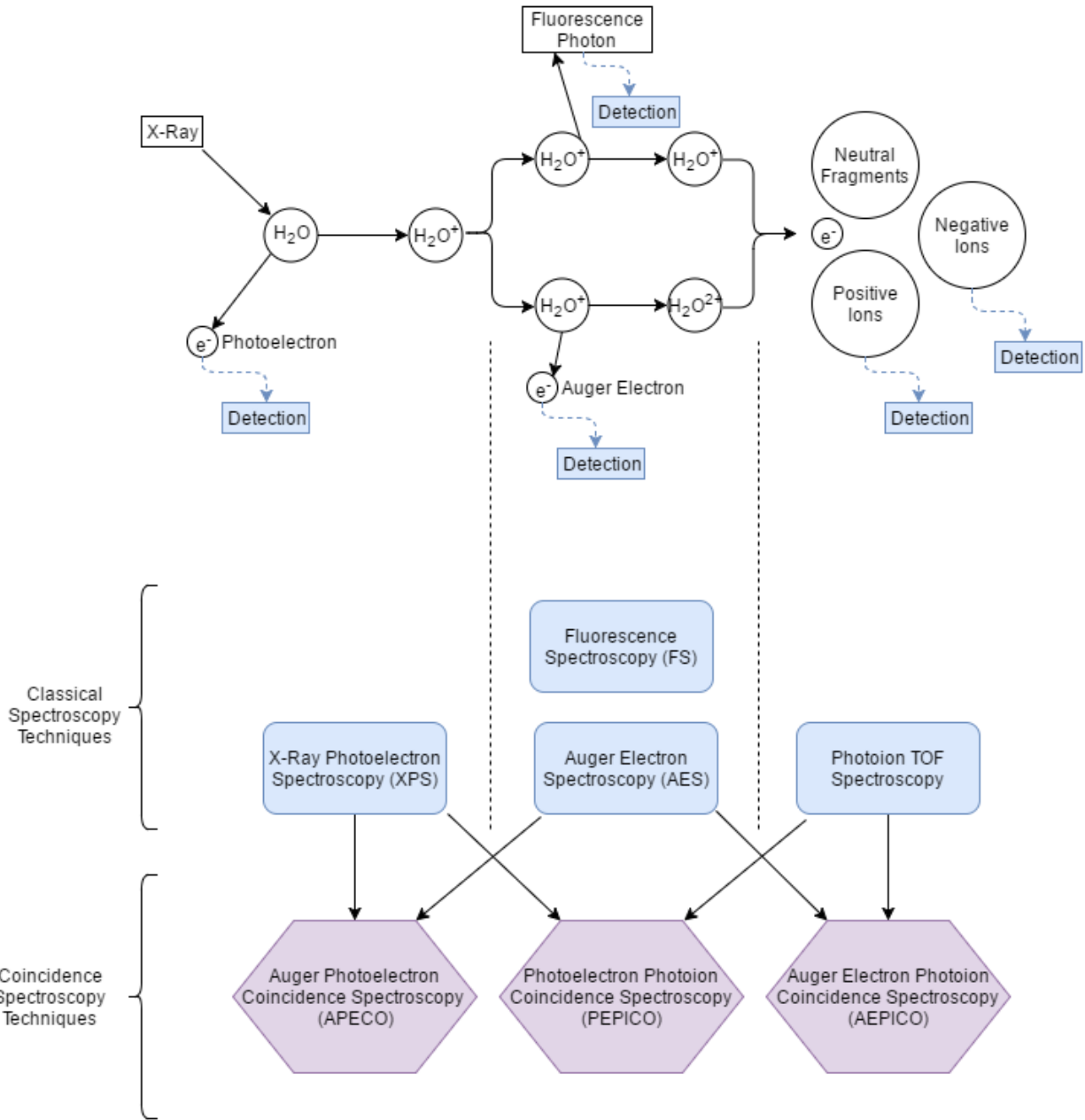
Figure 7: The different stages following core shell X-ray ionization, examples of associated spectroscopy techniques and their potential use in coincidence spectroscopy.

the processes occurring in Auger excitation and decay for a number of molecules and atoms, such as oxygen[22]. Similarly, multi-electron coincidence was used to investigate the double Auger effect[7]. The positive ions and the electrons produced in the dissociation process also have been used in Photoelectron Photoion Coincidence (PEPICO) and Auger Electron Pho-

toion Coincidence (AEPICO), to provide deeper understanding of dissociation mechanisms of water[23]. Finally, positive ions and negative ions have been detected in coincidence spectroscopy as well[3]. In particular, a recent Positive Ion/Negative Ion coincidence (NIPICO) setup has been successfully implemented and used to study the dissociation pathways of water at the Gas Phase photoemission beamline of the Elettra synchrotron[24]. This setup is the one that has been modified for this work.

3.5 The pre-existing coincidence setup

The pre-existing NIPICO setup at the Gas Phase photoemission beamline contains two Wiley-McLaren ion TOF spectrometers built in alignment on opposite sides of the interaction region. One of them is a positive ion spectrometer known as RamiTOF and the other is a negative ion spectrometer known as ChristianTOF. They both share the same extractor/repeller, the extractor for one is the repeller for the other and vice versa.

The negative ion spectrometer has been designed with two permanent magnets on opposite sides of the drift section, as can be seen in Figure 8. These magnets are used in order to deflect most of the electrons produced by the ionization process and prevent them from reaching the rest of the TOF spectrometer and eventually the detector. Because the negative ions are much heavier than the electrons, their momentum is higher, and for a carefully selected magnetic field (in this case $15 \cdot 10^{-4}$T) the impact on negative ions time-of-flight is negligible. However, this method remains a compromise, as the fastest electrons, such as Auger electrons, can still manage to pass through the magnetic field[24].

The detectors in the RamiTOF and the ChristianTOF spectrometers are made from triply and doubly stacked Microchannel plates (MCP) respectively, the MCPs in each detector are connected in series. Incoming particles create an electron cascade in the first MCP, that is then transferred to the next MCP in the stack. The amplified signal is finally picked up by the anode to be measured. This requires a voltage cascade being established from the front of the first MCP through to the anode behind the last MCP.

A custom made needle is precisely positioned to inject gaseous samples in the interaction

region, crossing the photon beam. The pressure within the chamber, measured using a cold cathode gauge, without sample introduction is maintained in the 10^{-7}mbar range. With the gas inlet turned on, the pressure is increased up to the 10^{-6}mbar range. The gold meshes used in the setup to separate different regions in the spectrometers are obtained from Precision Eforming (28wires/cm, 18μm wire diameter, and 90% transmission efficiency)[25]. A photodiode is also placed in the path of the beam past the interaction region in order to scale the data collected, as the intensity of the beam is not constant across the whole energy range. Discriminators for both the start and stop channels are used to distinguish real signals from random noise.

3.6   Changes of the coincidence setup

The new short ABC extension is designed to replace the positive ion spectrometer RamiTOF, so as to offer a flexible array of coincidence spectroscopy techniques, such as AENICO and high-momentum PINICO, with a particular focus on XENICO. The pre-existing negative ion ChristianTOF is still used for negative ion detection or can have its potentials reversed to enable positive ion detection, making this setup extremely versatile.

The detector of the ABC extension is only able to detect a very small geometrical fraction of the emitted photons. The detector is placed as close as possible to the interaction region (approximately 34mm), so as to maximize the acceptance angle of these particles. This provides the detector with an acceptance angle of 0.39sr, which represents only 3% of a sphere. In addition, the presence of several gold meshes on the particle path reduces that fraction further. A polymide filter was initially placed in front of the detector for XENICO, so as to allow X-ray photons through and block any other particles.

3.6.1   Design of the detector

The detector used in the ABC extension is a Secondary Electron Multiplier (SEM-7M) from Baspik. In thickness, it is composed of a mesh, two stacked MCPs in series followed by an anode used to pick up the electric output of the stacked MCPs[26]. It has one connection to

21

the detector mesh in the front, one to the anode in the back and four intermediate pins, one for the front and back of each MCP.

The input pin of the second MCP was broken near its base, which prevented standard connections from being established between the output (back) of the first MCP and the input (front) of the second MCP. Since a small part of the pin still protruded from the ceramic, a fix was implemented by using a thin strip of carbon conductive tape to make the connection in place of standard wires. As the resistance across that thin strip of carbon tape was in the $10\text{M}\Omega$ range, it should be negligible in front of the MCPs resistance that was measured to be $120\text{M}\Omega$ per MCP.

3.6.2   Testing of the coincidence setup

First, the coincidence setup was tested for X-ray Emission/Positive Ion Coincidence (XEPICO) on neon. This was made possible by reversing the polarity of the ChristianTOF, thus enabling it to detect positive ions. This $h\nu/\text{Ne}^+$ coincidence experiment was performed at 868.04eV, the measured location of the $1s \rightarrow 3p$ photoexcitation peak of neon. Once coincidence peaks were successfully obtained, the sample was switched from Neon to sulfur hexafluoride, SF_6. Sulfur hexafluoride is known to produce negative ions and the 1s core hole of fluorine is known to decay (in measurable amount) by fluorescence. The polarity of the ChristianTOF was reversed back to its original settings to allow negative ion detection, effectively resulting in a XENICO setup. A coincidence measurement was performed at 688.0eV, the measured location of the $F1s \rightarrow a_{1g}$ resonance peak of SF_6. However, the fluorescence yield for SF_6 was not sufficient for coincidence peaks to appear. Considering that, according to data presented in Figure 6, the likelihood of fluorescence decay for water is even lower than what it is for sulfur hexafluoride, it was concluded that obtaining significant XENICO results on water would require very long measurement times with no guarantee of results. As a consequence, the polymide filter was removed and the focus of the coincidence experiments on water was shifted from XENICO to PINICO and AENICO on water. XENICO would have enabled to obtain interesting insight into fluorescence decay, which is rarer than Auger decay

for the water molecule. However, as coincidence spectroscopy techniques provide complimentary information, AENICO and PINICO are interesting alternatives. Indeed, AENICO represents the counterpart of XENICO the same way Auger decay is the counterpart of fluorescence decay, and PINICO can be used to confirm and build upon the results obtained in earlier work[3]. In particular, due to the proximity of the detector to the interaction region, a higher positive ion yield is expected in the short extension compared to what was obtained in NIPICO with the previous coincidence setup, which could increase visibility for the above-threshold resonances. The experimental setup intended to test the ABC extension for PINICO is represented in Figure 8.
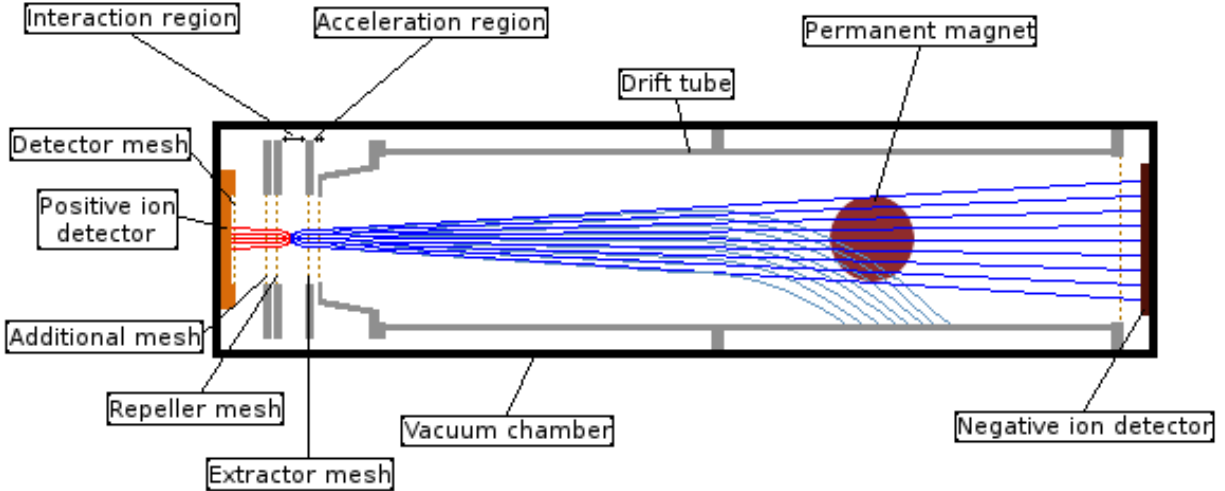
Figure 8: The experimental PINICO setup. Negative ion trajectories are represented in dark blue, electron trajectories are represented in light blue, Positive ion trajectories are represented in red.

3.6.3 Settings of the new coincidence setup

Because the ABC extension is much shorter than the ChristianTOF, it is easier to use positive ions rather than negative ions as the start signal for coincidence (positive ion triggering)[2]. Otherwise a temporal delay system would have to be introduced at the acquisition level for the negative ions to still produce the start signal. A third alternative, used in the previous setup would have been to use an external trigger as the start signal, such as a 10Hz pulse,

collect stop signals from both detectors separately and establish negative ion/positive ion coincidences later during the processing of the data (continuous triggering). The additional mesh inserted between the detector mesh and the extractor of the ABC extension enables to reduce the large potential drop that would otherwise be maintained between the extractor and the detector mesh. Tuning the potential applied to it allows to modify the time of the start signal with respect to the stop signal, and therefore should enable to distinguish real coincidence peaks from spurious peaks in the recorded spectrum, similarly to what can be done with the drift tube potential in the negative ion TOF spectrometer. The two permanent magnets used to divert the electrons travelling in the ChristianTOF drift tube were optimized in terms of position and a third magnet was introduced to minimize the number of (assumed) electron counts at the detector. Because of the relatively large number of electrons, it is likely that their contribution to the detector signal may have been larger than the actual negative ions contribution.

The potential cascade across the detector of the ABC extension is established via a voltage divider box, which implies that the nominal voltages it provides depend on the resistances in the box being much smaller than the resistance across the MCP detector. The potential cascade across the ChristianTOF was implemented using floating power supplies in series, with the first one being grounded and used as a reference. All other sources of potential were provided using grounded power sources. The input from the power sources that were directed at the ChristianTOF detector were filtered using low-pass filters to reduce noise and improve signal quality. High-pass filters were used at the anodes of both detectors to extract signal pulses and remove any high potential from the discriminator inputs. The voltages used for the PINICO setup are displayed in Table 1.

The distilled water used as a sample was prepared by using freeze-pump-thaw cycling in order to remove all the residual gases from the sample container. The valve connecting it to the gas injection needle was then carefully opened so as the sample slowly evaporates and passes through the narrowly opened valve in gaseous phase. The valve was heated using electric heating tape above room temperature so as to avoid condensation. The pressure in

Table 1: Voltage settings used for PINICO

	ABC extension	ChristianTOF
Extractor/Repeller potential	- 351 V	+ 351 V
Additional mesh	- 350 V	None
Drift tube	None	+ 1400 V
Detector mesh	- 2204 V	None
MCP stack front	- 1874 V	+ 1250 V
MCP stack back	- 220 V	+ 3098 V
Anode	Ground	+ 3298 V

the chamber, once it stabilized, was $2.6 \cdot 10^{-6}$mbar.

4   Results and discussion

4.1   Negative ion and positive ion yields

Prior to the coincidence experiment, the yield at each detector was quantified in order to check that the MCP detectors were in working order and detecting what they were meant to. Electron yield at the ChristianTOF detector (without magnets, it also includes negative ions) was in the 10^4Hz range, the negative ion yield (with the magnets in place removing most of the electrons) was in the 10^2Hz range and the positive ion yield at the ABC extension detector was in the 10^3Hz range, all were well above their respective background readings when the beamline was closed. Then, the photon energy of the beamline was scanned over the desired range and the signals from both MCP detectors were recorded to check the consistency of the indirect absorption spectrum with previous work. In the case of O1s core photoexcitation and photoionization of the water molecule, the adequate energy range is approximately 533eV to 550eV, as the first O1s photoexcitation of the water molecule to the unoccupied orbital $4a_1$ occurs at 533.96eV and the ionization threshold is located at 539.9eV[27, 28].

The recorded detector signals of both the ABC extension for positive ions and the ChristianTOF for negative ions (alongside electrons that are detected in spite of the filtering magnetic field) are shown in Figure 9. The below ionization threshold parts of the spectrum

can be identified, with clearly defined photoexcitation peaks for the $1Os \rightarrow 4a_1$ resonance at 533.96eV, for the $1Os \rightarrow 2b_2$ resonance at 535.98eV and for the $1Os \rightarrow 2b_1$ resonance at 537.04eV. The photon energy scale was calibrated according to the $O1s \rightarrow 4a_1$ excitation energy of 533.96eV from Hjelte *et al.*[29]. The 1.9eV spacing between the $4a_1$ and $2b_2$ peaks, and the 1.17eV spacing between the $2b_2$ and $1b_1$ peaks, as well a their height and shape are consistent with previous work[3, 27]. Weaker photoexcitation peaks are also discernible at 537.83eV and 538.53eV, before the above threshold region starting at 539.9eV. As expected, the negative ion yield is much lower than the positive ion yield. It can be estimated from Figure 9 to be approximately 50 times lower. However, this negative ion yield may still mostly be due to electrons than negative ions. The photoexcitation resonances and the signal behavior above threshold can be observed in the negative ion yield as well as in the positive ion yield, in spite of the lower signal to noise ratio.
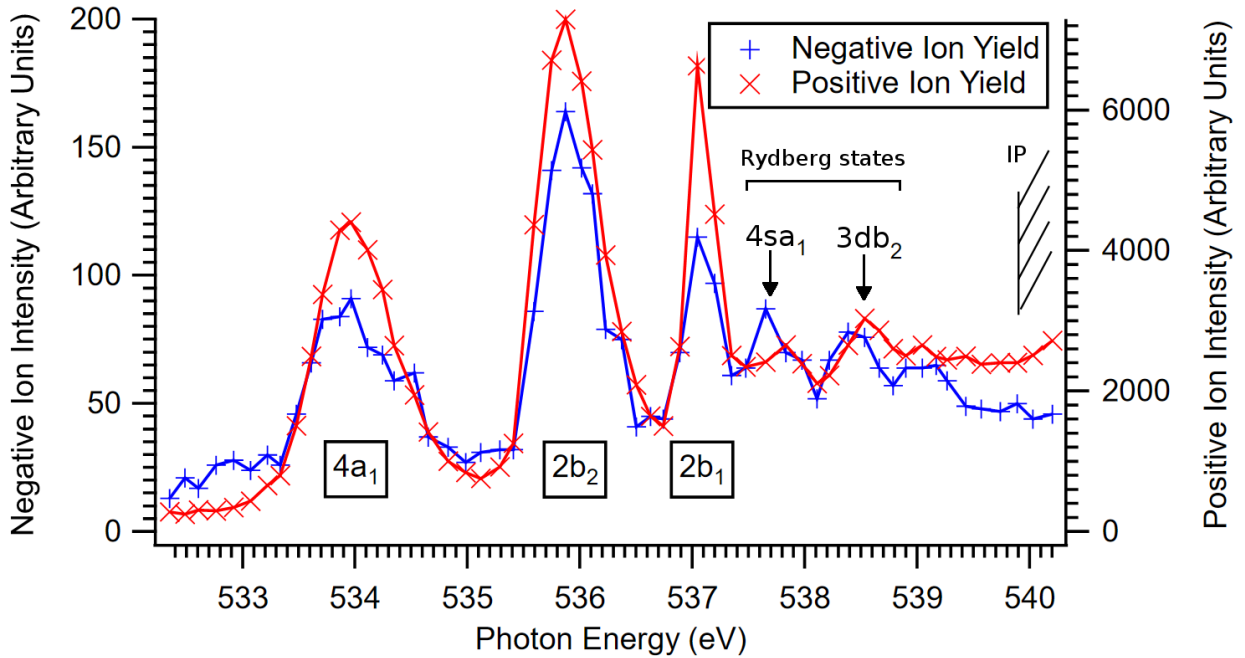

Figure 9: Positive ion yield and negative ion yield recorded at the ABC extension detector and the ChristianTOF detector. Scale is given separately for each yield due the large difference in magnitude between the negative ion yield and the positive ion yield.

4.2   Positive Ion/Negative Ion Coincidence (PINICO)

The coincidence spectrum measured based on this setup is recorded at the $2b_2$ excitation peak at 535.96eV, and the measured spectrum is plotted in Figure 10. The real or spurious nature of the observed peaks is determined by whether they move when changing the voltage of the drift tube of the ChristianTOF or the additional mesh of the ABC extension, as can be seen in Figure 11.
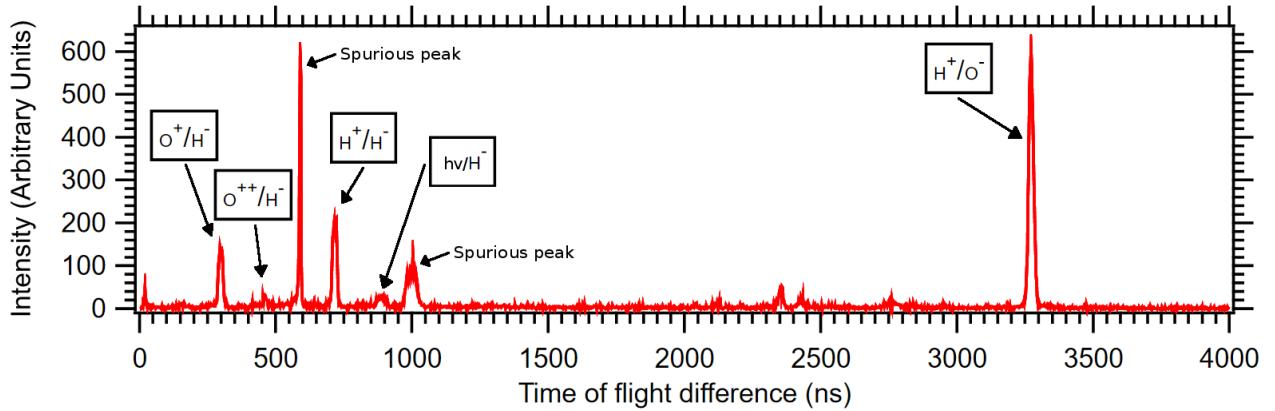
Figure 10: PINICO spectrum recorded using the ABC extension and the ChristianTOF at 535.98eV, which corresponds to the location of the $1Os \rightarrow 2b_2$ photoexcitation peak.
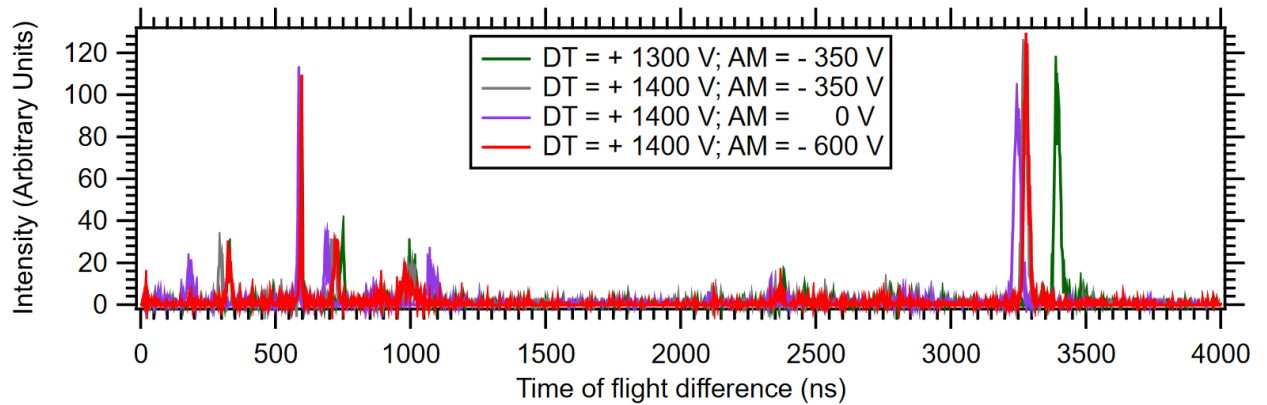
Figure 11: Position shifts used to distinguish real peaks from spurious peaks by changing the drift tube and the additional mesh voltages. DT stands for the voltage applied to the drift tube and AM for the voltage applied to the additional mesh.

The applied voltages were varied in 100V steps for the drift tube and in ~ 300V steps for the additional mesh, because the time-of-flight is much shorter in the ABC extension, and as

27

a consequence, the applied voltages required to obtain similar variations in time are higher. When the potential applied to the additional mesh is kept constant, a lower potential at the drift tube increases the time-of-flight of the negative ions, resulting in the real coincidence peaks being shifted toward longer time differences, and shorter time differences for a higher potential. Similarly, when the potential applied to the drift tube is kept constant, a lower potential at the additional mesh increases the time-of-flight of the positive ions, resulting in the real coincidence peaks being shifted towards shorter time differences, and longer time differences for a higher potential. The peaks that shifted consistently with this prediction were considered real and the others spurious. The thus identified real peaks locations are, from lowest to highest time of flight difference: 300ns, 700ns and 3270ns.

Assignment of the peaks is shown in Figure 10. The real peak located at 3270ns should correspond to the longest time difference, between the fastest positive ion and the slowest negative ion: H^+/O^-. The fact that it is the strongest coincidence peak is in agreement with earlier work[3]. At 700ns is another well defined real peak, which can be attributed to the H^+/H^- coincidence. The last clearly visible real peak in the spectrum at 300ns should therefore be O^+/H^-. It has a very short time of flight difference since the start signal is given by O^+, a slow positive ion and the stop by H^-, a fast negative ion. In addition, a small peak may be attributed to the O^{++}/H^- coincidence at 450ns, the O^{++} ion being faster than the O^+ ion but slower than the H^+ ions. The assignment of these peaks is consistent with their expected height, assuming negative charges are more likely to be carried by the oxygen atom and positive charges are more likely to be carried by the hydrogen atoms.

The small peak at 875ns or the broad peak at 1000ns may potentially be attributed to coincidence involving H^-, like the real peaks close to it. However, their longer time difference would denote an even faster start signal than the H^+/H^- peak. As such, the start signal might be attributed to photons. Which of these two is more likely to be the $h\nu/H^-$ coincidence peak can be determined by using the formula $t = \frac{d}{\sqrt{2U}} \cdot \sqrt{m/q}$ from Ch. 3.3, and the attribution of two H^- coincidence peaks. For the O^+/H^- coincidence, $\sqrt{16/1} = 4 \cdot \frac{d}{\sqrt{2U}} = X - 300$ns, and for the H^+/H^- coincidence, $\sqrt{1/1} \cdot \frac{d}{\sqrt{2U}} = X - 700$ns, where X stands for the reference time,

which corresponds to the time of flight of the H^- and is the same in both cases. Solving these two equations, the value of the parameters can be obtained: $\frac{d}{\sqrt{2U}} = 133.3\text{ns} \cdot A_r^{-1/2} \cdot e^{1/2}$ and $X = 833.3\text{ns}$. These parameters predict the position of the O^{++}/H^- peak to be 456ns, which is close to the 450ns experimental value, and the $h\nu/H^-$ coincidence (assuming instantaneous detection of photons) is predicted at $X = 833.3\text{ns}$ which may correspond to the small peak at 875ns, but not the broad peak at 1000ns.

It is interesting to see that with this set-up, the H^+/e^-, O^+/e^- and OH^+/e^- coincidences, seen in the earlier study by Stråhlman *et al.*, are not visible. This can be explained by the start signal being provided by slow positive ions (O^+ and OH^+) while the stop signal is provided by very fast electrons. It is likely then that the stop signal for these coincidences occurs before the start signal. It would be possible to set a delay in the acquisition system to be able to record them if these coincidences become of interest. Otherwise, continuous triggering may be used to record all hits, followed by computer analysis to establish the coincidences at a later stage. The other peaks, including the broad peak located at 1000ns are highly insensitive to voltage changes and are considered spurious peaks that arise from undesired processes, problems in the setup, the electronics, or cross-talk between the detectors[3].

4.3   Energy dependant ion pair production

The photon energy was scanned from 532.3eV to 540.7eV in 0.15 eV steps taking 600s long measurements for each data point. The intensity in each correctly identified coincidence peak was integrated and that value was plotted against energy, thus enabling PINICO yield per ion coincidence pair as a function of energy, as illustrated in Figure 12. To compensate for the intensity of the beam not being constant across all photon energies, the output of the photodiode was used to scale each corresponding data point. In Figure 12, the relative height of the peaks from each graph provides information about photoexcitation to different unoccupied orbitals in terms of ionic fragmentation probabilities.

Most of the spectra have very similar relative difference between photoexcitation peaks, showing approximately a 60% increase between the $4a_1$ and the $2b_1$ peaks and a slight drop
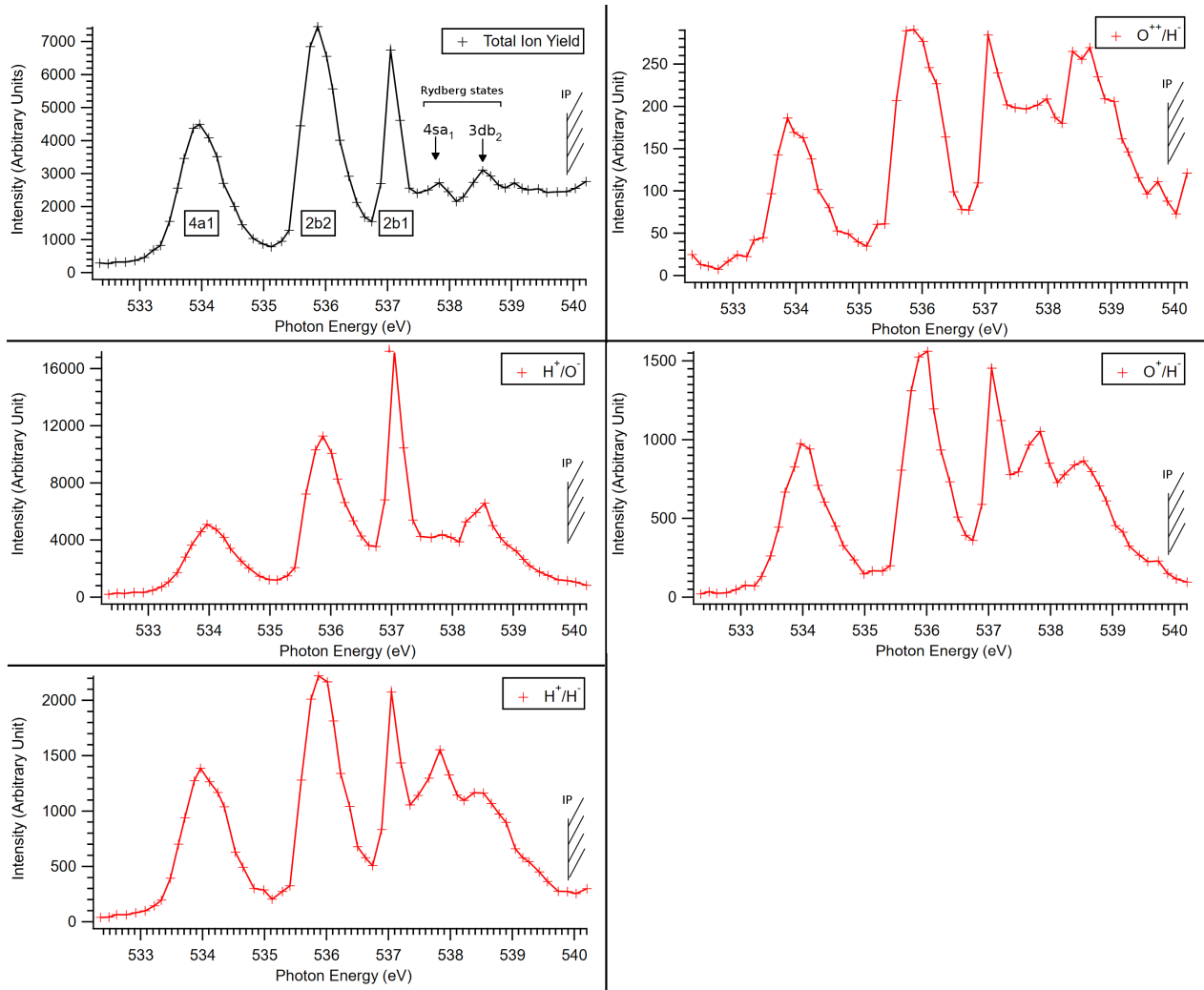
Figure 12: Integrated PINICO yield of each detected ion pair over the photon energy range corresponding to water core excitations. Total ion yield is provided for comparison.

of at most 7% between the $2b_1$ and the $2b_2$ peaks. The only exception to this general pattern is the H^+/O^- spectrum, where the $4a_1/2b_1$ peak height difference is approximately 120%, which is twice of what it is for the other spectra. The $2b_1/2b_2$ difference is also unusual, showing a considerably large increase of 53% instead of the expected slight decrease. This may be caused by a suppression of the $1a_1 \rightarrow 4a_1$ resonance with respect to the $1a_1 \rightarrow 2b_2$ resonance. The same behavior was observed by Ҡrӡhlman *et al.*, but it was noticeably greater for their Negative Ion/Positive Ion/Positive Ion Coincidence (NIPIPICO) measurement of

$O^-/H^+/H^+$ than it was for their NIPICO measurement of O^-/H^+. They then suggested that a large proportion of the O^-/H^+ coincidences at the $4a_1$ resonance could be due to radiative decay[3]. Assuming the probability of radiative decay is independent of photon energy, and that it is as unlikely for water as Figure 6 suggests, this relative suppression would mean that the nonradiative (Auger) decay is less likely to produce this ion pair at this particular resonance than at the $1b_1$ or $2b_2$ resonances, which would deserve further investigation. This behavior can be linked to the exceptional character of the H^+/O^- coincidence. Indeed, this dissociation is the most likely, because of the high electronegativity of oxygen to that of hydrogen. This is also reflected in the high number of overall counts for this ion pair produced coincidentally.

Considering the discussion in Ch. 2.1 about potential ion fragmentation channels for resonant or normal Auger decay, a few additional observations can be made about results shown in Figure 12. Namely, the O^{++}/H^- ion pair production may occur via $H_2O^{+*} \rightarrow H^- + O^{++} + H$ at resonance, which is an unlikely scenario from an energetic standpoint, as the electronegative oxygen would have not taken any valence electron from either hydrogen atoms (which is why none carry a positive charge), but instead have an additional electron removed during the dissociation process, forming a H^- ion. Above threshold, however, the signal can stay relatively high via $H_2O^{2+*} \rightarrow H^- + O^{++} + H^+$, a dissociation pathway following normal Auger decay which has a higher chance of removing two electrons from the oxygen atom than its resonant counterpart. Indeed, since the initial charge is higher, there are less electrons available to stay with the oxygen atom after dissociation. This contrasts the fact that in the case of resonant Auger decay, there is still the possibility for readjustments of the electronic orbitals before dissociation. The relatively high value of the O^{++}/H^- above threshold yield to that of its photoexcitation resonance peaks is in agreement with this prediction. The resemblance of the H^+/H^- and O^+/H^- graphs is consistent with the idea that above threshold variations of the H^- yield are not responsible for the behavior of the O^{++}/H^- graph. At this point, it would be useful to use NIPIPICO to distinguish the different pathways more accurately. However, this would require the use of continuous triggering, as described in Ch.

3.6.3 instead of the start signal being provided by positive ions.

O^-/H^+ ion pairs should also show a low production rate in the above threshold region, as the $H_2O^{+*} \rightarrow H^+ + O^- + H^+$ pathway is the only one capable of producing O^- in a simple dissociation following resonant Auger decay. This can be determined to be the case from the only 3.7 times higher count rate experienced above threshold to that of below threshold for this ion pair. Compared to the same ratio taken from the other PINICO pairs (6.4 for H^+/H^-, 4.8 for O^+/H^- and 5.0 for O^{++}/H^-), the H^+/O^- pair seems to be the least common above threshold relative to its abundance below threshold, as expected.

The relative strength of Rydberg resonances, especially the $3db_2$ resonance, for the O^{++}/H^- yield is greater than for the other ion pairs, with intensities comparable to the peak value of the 2b1 resonance. This relative strength can be partially explained by the lower signal to noise ratio for this rare ion pair, but it deserves further study. In particular, longer measurement times would enable to verify whether this exceptional strength of the Rydberg resonances for the O^{++}/H^- ion pair yield is an artifact.

4.4 PINICO events above O1s ionization threshold

The above threshold part of the spectrum (540eV to 567eV) was measured separately, taking 0.4eV steps and measuring for 600s at each energy. The results displayed in Figure 13 are produced by integrating each coincidence peak over photon energy and scaling for intensity in the same way as what was done for Figure 12. A clearly defined broad resonance can be seen at ~556eV for H^+/H^-, O^+/H^- and possibly O^{++}/H^-, although for the latter, the low number of counts makes a potential peak difficult to distinguish from background noise. There is a similar resonance for the remaining H^+/O^- in the above threshold spectrum, but it shows structure that seems to result from two broad peaks at 550eV and 554eV overlapping. It can be conjectured that the broad resonances for the other ion pairs also possess structure, but they are not visible due to the low signal to noise ratio, a tighter peak structure or a combination of both.

These resonances have been observed in earlier works by electron impact and fluorescence
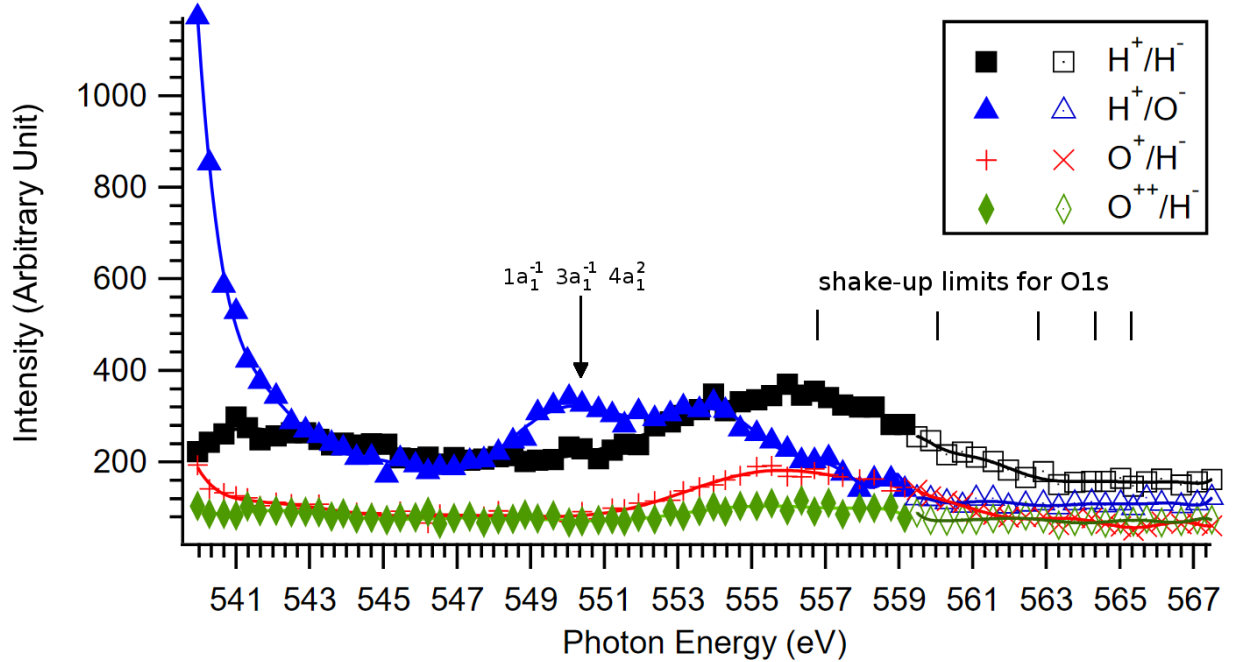
Figure 13: Integrated PINICO yield of each available ion pair above threshold measured for core excited water. The shake-up limits were obtained from [30].

emission spectroscopy, and attributed to the simultaneous excitation of a core electron in the $1a_1$ shell and an electron from an occupied valence shell (shake-up)[31, 32]. In particular, the double peak structure of the H^+/O^- coincidence spectrum is very similar to what was observed by Kivimäki *et al.* in their photoabsorption spectrum above the O1s edge of water[32]. The energy of the $1a_1 \to 4a_1$ excitation added to energy of the $3a_1 \to 4a_1$ shake up[30] give $533.96eV + 16.96eV = 550.92eV$. This should be the lowest energy at which these simultaneous excitations occur, resulting in a $1a_1^{-1}3a_1^{-1}4a_1^2$ state. Even taking into account the error due to considering each excitation to occur independently from one another, this value is very close to the observed peak at 550eV. The position and range of these previously observed resonances seem to coincide with the ones in Figure 13. A similar broad feature for the O^+/H^- coincidence spectrum has already been observed by Stråhlman *et al.* with the water molecule, but the above threshold resonances of other ion pairs measured here were not visible[3]. Stolte *et al.* had also previously observed a clearly defined O^- ion yield resonance at 550eV, although this resonance was lying on the edge of their energy range, and was

33

not measured in its entirety[33]. A high loss of H^+ ions with a large transverse momentum was suggested by Stråhlman *et al.* for the absence of a H^+/O^- resonance at 550eV in their above threshold spectrum. This explanation would also hold for the other above threshold resonances for ion pairs involving H^+ that they did not observe. In the case of this experiment, the close proximity of the ABC extension to the interaction region would compensate for H^+ ions transverse momentum, which is consistent with the high-loss hypothesis in the pre-existing RamiTOF.

The relatively lower energy at which this broad resonance appears for H^+/O^- compared to the other ion pairs might be explained by the scan in excitation energies that occurs for the valence shell electrons. Indeed, as energy increases and the resonance starts to appear, the energy available for valence shell excitation increases and should scan through the valence orbitals, starting from the shallowest one down towards the deepest valence orbitals. Considering that the outer valence shell electrons are more involved in bonding, and are statistically farther from the oxygen atom, their excitation would have higher chances of resulting O^- ions after dissociation. The excitation of deeper valence orbitals would have the opposite effect. This would explain the earlier resonance for the H^+/O^- ion pair observed in Figure 13.

5 Outlook

The newly developed ABC extension greatly increased the versatility of the setup. It presents an advantage over the positive ion TOF that it replaced for PINICO, as the shorter time of flight reduces high-momentum light positive ion losses, which may be essential in TOFMS for hydrogen rich molecules. However, this increase in ion yield is obtained at the expense of resolution on the positive ion side, also due to the shorter time-of flight. NIPIPICO could be provided by either delaying the signal from the ABC extension detector, which would allow to use the negative ion detection as the start signal, or using continuous triggering. The voltages can be adjusted for Auger electron detection, by deflecting low energy electrons, which would

allow for AENICO or AEPICO, depending on the voltages applied to the ChristianTOF. A filter can be introduced after the additional mesh, in order to block fragments from reaching the detector, and enable XENICO or XEPICO. The crude magnets used to divert electrons in the ChristianTOF could be replaced by electromagnets in the chamber, which would enable to tune electron filtering more precisely and increase overall performance of the setup. The lack of a preferred direction for the emission of photons could be used to position one or several photon detectors on the periphery of the cylinder defined by the extractor and repeller meshes. That would bring the detectors closer to the interaction region, with a potentially a larger combined surface area, while freeing the ABC extension for positive ion or Auger electron detection. The ABC Extension could also be replaced by a longer positive ion TOF that compensates for the transverse momentum of light positive ions (in this case H^+ ions) using electrostatic lenses. Simulations should be performed on both the ABC Extension and the longer positive ion TOF featuring electrostatic lenses in order to ensure that the latter is a superior alternative in terms of collection efficiency.

This experimental setup provides interesting information about the ionic dissociation pathways of the water molecule above threshold with PINICO, which confirmed observations made in earlier work, as well as add new information that can be used to motivate further investigation of the dissociation pathways of the water molecule via coincidence spectroscopy. In particular, it showed the existence of ion-pair dependant measurable resonances in the above ionization threshold coincidence spectrum of water, attributed by earlier work to simultaneous excitation of both a core electron and a valence electron.

References

[1] Y. Maréchal. *The Hydrogen Bond and the Water Molecule.* Elsevier, 2007. ISBN 978-0-444-51957-3.

[2] C. Stråhlman, R. Sankari, A. Kivimäki, R. Richter, M. Coreno, and Ralf Nyholm. A tandem time-of-flight spectrometer for Negative-Ion/Positive-Ion coincidence measure-

ments with soft X-ray excitation. *Review of Scientific Instruments*, 87:013109, 2016. doi: 10.1063/1.4940425.

[3] C. Strahlman, A. Kivimaki, R. Richter, and R. Sankari. Negative-Ion/Positive-Ion coincidence yields of core-excited water. *The Journal of Physical Chemistry*, 120:6389–6393, 2016. doi: 10.1021/acs.jpca.6b06207.

[4] J. M. Hollas. *Basic Atomic and Molecular Spectroscopy*. Royal Society of Chemistry, 1st edition, 2002. ISBN 978-0-85404-667-6.

[5] H. Siegbahn, L. Asplund, and P. Kelfve. The Auger electron spectrum of water vapour. *Chemical Physics Letters*, 35(3):330–335, 1975. doi: 10.1016/0009-2614(75)85615-6.

[6] K. Siegbahn. *ESCA Applied to Free Molecules*. North Holland/American Elsevier, 1st edition, 1969. ISBN 0720401607.

[7] M. Mucke, J.H.D. Eland, O. Takahashi, P. Linusson, D. Lebrun, K. Ueda, and R. Feifel. Formation and decay of core-orbital vacancies in the water molecule. *Chemical Physics Letters*, (558):82–87, 2013. doi: 10.1016/j.cplett.2012.11.094.

[8] P. Willmott. *An Introduction to Synchrotron Radiation: Techniques and Applications*. John Wiley Sons, 1st edition, 2011. ISBN 9780470745793.

[9] S. Svanberg. *Atomic and Molecular Spectroscopy: Basic Aspects and Practical Applications*. Springer, 3rd edition, 2001. ISBN 9783642981074.

[10] A. Naves de Brito, R. Feifel, A. Mocellin, A.B. Machado, S. Sundin, I. Hjelte, S.L. Sorensen, and O. Björneholm. Femtosecond dissociation dynamics of core-excited molecular water. *Chemical Physics Letters*, (309):377–385, 1999. doi: 10.1016/S0009-2614(99)00693-4.

[11] R. Manne. Molecular orbital interpretation of Xray emission spectra: simple hydrocarbons and carbon oxides. *The Journal of Chemical Physics*, 52(11):5733–5739, 1970. doi: 10.1063/1.1672852.

[12] W. Bambynek, B. Crasemann, R. W. Fink, H.-U. Freund, Hans Mark, C. D. Swift, R. E. Price, and P. Venugopala Rao. X-ray fluorescence yields, Auger, and Coster-Kroning transition probabilities. *Review of Modern Physics*, 44(4):716–813, 1972. doi: 10.1103/RevModPhys.44.716.

[13] C.G. Ning, B. Hajgató, Y.R. Huang, S.F. Zhang, K. Liu, Z.H. Luo, S. Knippenberg, J.K. Deng, and M.S. Deleuze. High resolution electron momentum spectroscopy of the valence orbitals of water. *Chemical Physics*, (343):19–30, 2008. doi: 10.1016/j.chemphys. 2007.09.030.

[14] J. Nordgren, L. 0. Werme, H. Agren, C. Nordling, and K. Siegbahn. The X-ray emission spectrum of water. *Journal of Physics B: Atomic, Molecular and Optical Physics*, 8(2): L18–L19, 1975. doi: 10.1088/0022-3700/8/2/003.

[15] S. Kashtanov, A. Augustsson, Y. Luo, J.-H. Guo, C. Såthe, J.-E. Rubensson, H. Siegbahn, J. Nordgren, and H. Ågren. Local structures of liquid water studied by x-ray emission spectroscopy. *Physical Review*, (69):024201, 2004. doi: 10.1103/PhysRevB.69. 024201.

[16] Elettra and fermi lightsources. `http://www.elettra.eu/`. Accessed: 2016-09-27.

[17] K. C. Prince, R. R. Blyth, R. Delaunay, M. Zitnik, J. Krempasky, J. Slezak, R. Camilloni, L. Avaldi, M. Coreno, G. Stefani, C. Furlani, M. de Simone, and S. Stranges. The Gas-phase photoemission beamline at Elettra. *Journal of Synchrotron Radiation*, 5:565–568, 1998. doi: 10.1107/S090904959800065X.

[18] R.R. Blyth, R. Delaunay, M. Zitnik, J. Krempasky, R. Krempaska, J. Slezak, K.C. Prince, R. Richter, M. Vondracek, R. Camilloni, L. Avaldi, M. Coreno, G. Stefani, C. Furlani, M. de Simone, S. Stranges, and M.-Y. Adam. The high resolution Gas-phase photoemission beamline, Elettra. *Journal of Electron Spectroscopy and Related Phenomena*, 101-103:959–964, 1999. doi: 10.1016/S0368-2048(98)00381-8.

[19] W. C. Wiley and I. H. McLaren. Time-of-flight mass spectrometer with improved resolution. *The Review of Scientific Instruments*, 26:1150–1157, 1955. doi: 10.1063/1.1715212.

[20] G. Sanzone. Energy resolution of the conventional time-of-flight mass spectrometer. *Review of Scientific Instruments*, 41:741–742, 1970. doi: 10.1063/1.1684631.

[21] O. Hemmers, S. B. Whitfield, P. Glans, H. Wang, D. W. Lindle, R. Wehlitz, and I. A. Sellin. High-resolution electron time-of-flight apparatus for the soft x-ray region. *Review of Scientific Instruments*, 69:3809–3817, 1998. doi: 10.1063/1.1149183.

[22] T. Arion, R. Püttner, C. Lupulescu, R. Ovsyannikov, M. Förstel, G. Öhrwall, A. Lindblad, K. Ueda, S. Svensson, A. M. Bradshaw, W. Eberhardt, and U. Hergenhahn. New insight into the Auger decay process in O_2: The coincidence perspective. *Journal of Electron Spectroscopy and Related Phenomena*, 185:234–243, 2012. doi: 10.1016/j.elspec. 2012.06.010.

[23] K. Norwood, A. Ali, and C. Y. Ng. A photoelectron-photoion coincidence study of $H_2 0$, $D_2 0$, and $(H_2 0)_2$. *The Journal of Chemical Physics*, 95:8029–8037, 1991. doi: 10.1063/1.461334.

[24] C. Stråhlman. *Time-of-Flight Ion and Electron Spectroscopy: Applications and Challenges at Storage Ring Light Sources.* PhD thesis, Lund University, PO Box 117 221 00 Lund +46 46-222 00 00, 01 2016. http://lup.lub.lu.se/record/8866027.

[25] Precision eforming. `http://www.precisioneforming.com/`. Accessed: 2016-11-25.

[26] Baspik vladikavkaz technological center. http://www.baspik.com/eng/. Accessed: 2016-11-01.

[27] J. Schirmer, A. B.Trofimov, K.J. Randall J. Feldhaus, A. M. Bradshaw, Y. Ma, C. T. Chen, and F. Sette. K-shell excitation of the water, ammonia, and methane molecules using high-resolution photoabsorption spectroscopy. *Physical Review A*, 47(2):1136–1147, 2003. doi: 10.1103/PhysRevA.27.2503.

[28] W.L. Jolly, K.D. Bomben, and C.J. Eyermann. Core-electron binding energies for gaseous atoms and molecules. *Atomic Data and Nuclear Data Tables*, 31(3):484, 1984. doi: 10.1016/0092-640X(84)90011-1.

[29] I. Hjelte, M.N. Piancastelliand R.F. Fink, O. Bjorneholm, M. Bassle ran dR. Feifel, A. Giertz, H. Wang, K. Wiesner, A. Ausmees, C. Miron, S.L. Sorensen, and S. Svensson. Evidence for ultra-fast dissociation of molecular water from resonant Auger spectroscopy. *Chemical Physics Letters*, 334:151–158, 2001. doi: 10.1016/S0009-2614(00)01434-2.

[30] R. Sankari, M. Ehara, H. Nakatsuji, A. De Fanis, H. Aksela, S.L. Sorensen, M.N. Piancastelli, E. Kukk, and K. Ueda. High resolution O 1s photoelectron shake-up satellite spectrum of H2O. *Chemical Physics Letters*, 124:51–57, 2006. doi: 10.1016/j.cplett.2006.02.018.

[31] G. R. Wight and C. E. Brion. K-shell excitation of CH, NH, H_2O, CH_2OH, CH_3OCH_3 and CH_3NH_2 by 2.5 keV electron impact. *Journal of Electron Spectroscopy and Related Phenomena*, 4:25–42, 1974. doi: 10.1016/0368-2048(74)80040-X.

[32] A. Kivimäki, M. de Simone, M. Coreno, V. Feyer, E. Melero García, J. Álvarez Ruiz, R. Richter, and K. C. Prince. Observation of core-hole double excitations in water using fluorescence spectroscopy. *Physical Review A*, 75:014503, 2007. doi: 10.1103/PhysRevA. 75.014503.

[33] W. C. Stolte, M. M. Sant'Anna, G. Ohrwall, M. N. Piancastelli, I. Dominguez-Lopez, and D. W. Lindle. Photofragmentation dynamics of core-excited water by anion-yield spectroscopy. *Physical Review A*, 68:022701, 2003. doi: 10.1103/PhysRevA.68.022701.